PROCEEDINGS OF SCIENCE

Electron and Positron Fluxes in Primary Cosmic Rays Measured with the Alpha Magnetic Spectrometer on the International Space Station

Nikolas Zimmermann[∗] **for the AMS collaboration**
Rheinisch-Westfälische Technische Hochschule (DE)
E-mail: `zimmermann@physik.rwth-aachen.de`

Precision measurements by the Alpha Magnetic Spectrometer on the International Space Station of the primary cosmic-ray electron flux in the range 0.5 to 700 GeV and the positron flux in the range 0.5 to 500 GeV are presented. The electron flux and the positron flux each require a description beyond a single power-law spectrum. Both the electron flux and the positron flux change their behavior at ~ 30 GeV but the fluxes are significantly different in their magnitude and energy dependence. Between 20 and 200 GeV the positron spectral index is significantly harder than the electron spectral index. The results show, for the first time, that neither e^+ nor e^- can be described by a single power law above 27.2 and 52.3 GeV, respectively. The determination of the differing behavior of the spectral indices versus energy is a new observation and provides important information on the origins of cosmic-ray electrons and positrons.

The European Physical Society Conference on High Energy Physics
22-29 July 2015
Vienna, Austria

PoS(EPS-HEP2015)400

[∗] Speaker.

We present measurements of the electron and positron fluxes in primary cosmic rays with the Alpha Magnetic Spectrometer (AMS-02) on the International Space Station (ISS). The measurements presented here are based on 41 billion triggered events collected between 19 May 2011 and 26 November 2013 and covers the energy range from 0.5 to 700 GeV for electrons and from 0.5 to 500 GeV for positrons.

AMS-02 is a general-purpose high-energy particle physics detector that was installed on the ISS in May 2011. AMS-02 has measured the positron fraction $e^+/(e^+ + e^-)$ as a function of energy in the range from 0.5 to 500 GeV and found that the positron fraction clearly rises towards high energies [1]. The results from AMS-02 on the positron fraction generated widespread interest and discussions on the origin of high energy positrons [2]. The precise measurements of the electron and positron fluxes as a function of energy offer detailed insight into the origin of cosmic rays. The AMS measurements of the combined $(e^+ + e^-)$ fluxes are discussed in [3].

These proceedings are an abbreviated version of the original AMS-02 publication [4].

1. The AMS-02 Detector

The AMS-02 detector [1, 5] consists of nine planes of precision silicon tracker, a transition radiation detector (TRD), four planes of time of flight counters (TOF), a permanent magnet, an array of anticoincidence counters (ACC), surrounding the inner tracker, a ring imaging Čerenkov detector (RICH), and an electromagnetic calorimeter (ECAL). AMS operates without interruption on the ISS and is monitored continuously from the ground. The timing, location and attitude of AMS are determined by a combination of GPS units affixed to AMS and to the ISS.

The tracker accurately determines the trajectory, momentum p, and absolute charge Z of cosmic rays by multiple measurements of the coordinates and energy loss. The coordinate resolution of each plane is measured to be better than $10\,\mu$m in the bending direction, and the charge resolution is $\Delta Z \approx 0.06$ at $Z = 1$. The maximum detectable rigidity of the full tracker, over a lever arm of 3 m, is ~ 2 TV.

The TRD uses transition radiation to distinguish between $e^\pm$ and protons. The signals from the 20 layers of proportional tubes are combined in a TRD likelihood that allows for separation of electrons and positrons from protons.

The ECAL spans 17 radiation lengths and measures the energy E of electrons and positrons. In the beam tests of the AMS detector, the energy resolution of the ECAL has been measured to be $\sigma(E)/E = \sqrt{(0.104)^2/(E/\mathrm{GeV}) + (0.014)^2}$. The three-dimensional shower shape is described by an ECAL estimator based on boosted decision trees [6].

The detector performance [1, 5] is steady over time. The entire detector has been extensively calibrated in a test beam at CERN with e^+ and e^- from 10 to 290 GeV/c, with protons at 180 and 400 GeV/c, and with $\pi^\pm$ from 10 to 180 GeV/c which produce transition radiation equivalent to protons up to 1.2 TeV/c. Measurements with 18 different energies and particles at 2000 positions were performed.

A full Geant 4.9.4 Monte Carlo (MC) simulation [7] of the complete AMS detector, including the digitization of the signals, is used for the analysis.

2. Data analysis

The isotropic flux of cosmic ray electrons ϕ_{e^-} or positrons ϕ_{e^+} in energy bins ΔE around energy E is given by

$$\phi_{e^\pm}(E) = \frac{N_{e^\pm}(E)}{A_{\text{eff}}(E)\cdot\varepsilon_{\text{trig}}(E)\cdot T(E)\cdot\Delta E} \tag{2.1}$$

with the number of electrons N_{e^-} or positrons N_{e^+} in the bin around energy E. The trigger efficiency is denoted by $\varepsilon_{\text{trig}}$, and T is the exposure time. The bin widths ΔE are chosen to be at least two times the energy resolution of the ECAL to minimize migration effects. With increasing energy the bin width becomes progressively larger to ensure adequate statistics in each bin. The effective acceptance is defined as

$$A_{\text{eff}} = A_{\text{geom}}\cdot\varepsilon_{\text{sel}}\cdot\varepsilon_{ID}\cdot(1+\delta), \tag{2.2}$$

where ε_{sel} is the selection efficiency and ε_{ID} is the identification efficiency for electrons and positrons. The geometrical acceptance of the detector components used in this analysis is calculated to be $A_{\text{geom}} = 550\,\text{cm}^2\,\text{sr}$. The product $A_{\text{geom}}\cdot\varepsilon_{\text{sel}}\cdot\varepsilon_{ID}$ is determined from the Monte Carlo simulation, and δ is a minor correction described below.

The absolute energy scale for this measurement is defined by the ECAL and determined by using minimum ionizing particles and the ratio E/p. These results are compared with the test beam values where the beam energy is known to high precision. This comparison limits the uncertainty of the absolute energy scale to 2% in the range covered by the beam test results, 10 - 290 GeV. Below this range, it increases to 5% at 0.5 GeV, above this range, it increases to 4% at 700 GeV. We treat this as an uncertainty of the bin boundaries.

The trigger efficiency $\varepsilon_{\text{trig}}$ is determined from data. The data acquisition system is triggered by energy depositions in all four TOF planes or the ECAL. In addition to these physics-triggered events, AMS records unbiased triggers requiring a coincidence of three out of the four TOF planes, from which the trigger efficiency can be calculated. $\varepsilon_{\text{trig}}$ is found to be 100% above 3 GeV decreasing to 75% at 1 GeV.

To reject secondary positrons and electrons produced by the interaction of primary cosmic rays with the atmosphere, the measured energy is required to exceed a cutoff. This cutoff is taken to be 1.2 times the maximum Stoermer cutoff [8] for either a positron or electron at the geomagnetic location where the particle was detected at any angle within the acceptance for the minimum energy particles within the bin. The exposure time $T(E)$ as a function of energy is determined by counting the livetime-weighted number of seconds at each geomagnetic location when detector operations were steady and the geomagnetic cutoff requirement is satisfied. This excludes TRD gas refills, time spent in the South Atlantic Anomaly and the time when the AMS z axis was more than 45° from the local zenith due to the orientation of the ISS. The exposure time $T(E)$ above 30 GeV is 6.1×10^7 seconds.

Events are selected by requiring the presence of a shower in the ECAL and tracks in the TRD and tracker. To identify down-going particles of charge $|Z| = 1$, cuts are applied on the velocity measured by the TOF system and on the charge reconstructed by the silicon tracker, upper TOF system, and TRD. The cut values are chosen to minimize the total error, defined as the quadratic sum of the statistical and systematic errors. The selection efficiency ε_{sel} is determined from the MC simulation. It is found to be a smooth function of energy with a value of $\sim 70\,\%$ at 100 GeV.

The identification of the e^- and e^+ signal requires rejection of the proton background. Cuts are applied on the E/p matching and the reconstructed depth of the shower maximum. This makes the negatively charged sample, as determined by the rigidity, a sample of pure electrons. A cut on the ECAL estimator is applied to further reduce the proton background in the positive rigidity sample after which the numbers of positrons and protons are comparable at all energies. The identification efficiency ε_{ID} is defined using the Monte Carlo simulation as the efficiency for electrons to pass these three cuts. It is identical for both electrons and positrons.

In order to determine the correction δ, a negative rigidity sample is selected for every cut using information from the detectors unrelated to that cut. The effects of the cut are compared between data and Monte Carlo simulation. This correction is found to be a smooth, slowly falling function of energy. It is $\sim 2\,\%$ at 10 GeV and $\sim 6\,\%$ at 700 GeV. The selection cut values and the identification cut values are chosen to maximize the measurement accuracy of the separate fluxes.

In each energy bin, a two-step fit procedure is performed to determine the number of positrons N_{e^+} and electrons N_{e^-}. First, the numbers of positrons and electrons reconstructed with a positive charge sign (N^+) or a negative charge sign (N^-) are determined. To this end, the distributions in the TRD likelihood for the positive and negative samples are parametrized as the sum of a signal and a background component. The shapes of the distributions for signal and background (so called "templates") are determined from ISS data, by selecting clean data samples of electrons and protons using the ECAL estimator and the charge sign measured by the tracker. The template for electrons and positrons does not depend on energy above 10 GeV. A maximum-likelihood fit of the templates to the data yields N^+, N^- and the number of protons in the sample. As an example, the result of the template fit in the positive event sample in the energy bin from 132 to 152 GeV is shown in Figure 1.

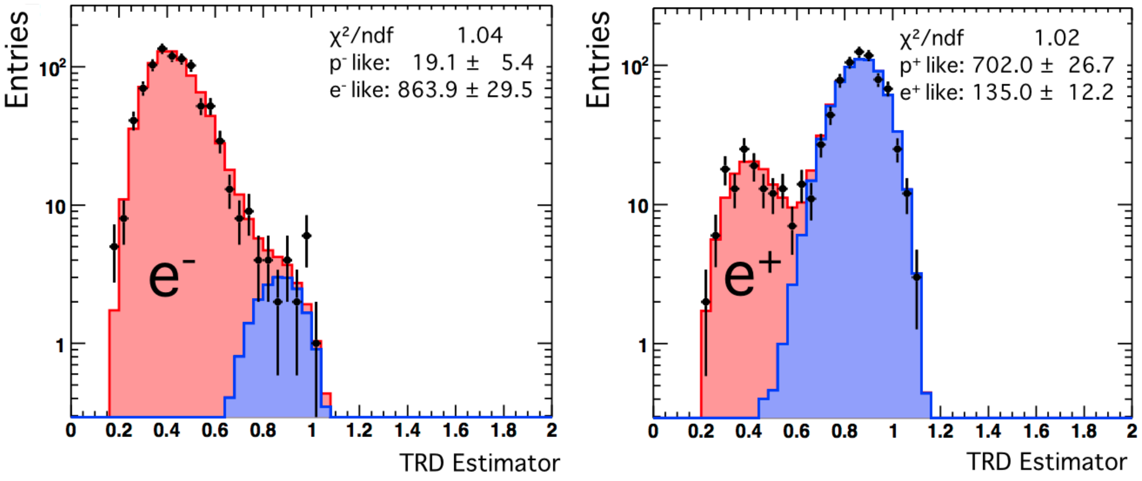

Figure 1: Fit results for the energy bin between 132 and 152 GeV, for events with, left: a negative reconstructed charge, right: a positive reconstructed charge. The best-fit contributions of signal and background are shown in red and blue, respectively.

Second, the values of N^+ and N^- determined in the first step are corrected for charge confusion to obtain N_{e^+} and N_{e^-}. Charge confusion occurs when an electron is reconstructed as a positron and vice versa. There are two main sources of charge confusion. The first is related to the finite resolution of the tracker and multiple scattering. The second is related to the production of secondary tracks along the path of the primary $e^\pm$ in the tracker. Charge confusion is determined using a dedicated estimator derived with a boosted decision tree technique which combines all the information from the tracker such as the track χ^2, the rigidity reconstructed using different sets of tracker layers, and the number of hits in the vicinity of the track. These tracker templates are fit to data, bin by bin, to obtain the amount of charge confusion resulting in the determination of N_{e^+} and N_{e^-}.

In total, 9.23 million events are identified as electrons and 0.58 million as positrons. These numbers are slightly less than the corresponding numbers from out positron fraction publication [1] due to tighter selection criteria for stringent control of the acceptance. For a detailed discussion of the systematic uncertainties please refer to our electron/positron paper publication [4].

3. Results

The electron and positron fluxes multiplied by E^3 are presented in Figure 2 together with the most recent measurements [9, 10] for comparison. Figure 3 shows the detailed behavior for both electrons and positrons below 200 GeV together with previous measurements [9, 10, 11, 12, 13, 14] in this energy range.

Below $\sim$10 GeV, the behavior for both electrons and positrons is affected by solar modulation as seen in our data by variations of the fluxes over this data-taking interval. However, above $\sim$20 GeV the effects of solar modulation are insignificant within the current experimental accuracy. The data show that above $\sim$20 GeV and up to 200 GeV the electron flux decreases more rapidly with energy than the positron flux, that is, the electron flux is softer than the positron flux. As seen in Figures 2 and 3, neither the electron flux nor the positron flux can be described by single power laws ($\propto E^\gamma$) over the entire range. To quantitatively examine the energy dependence of the fluxes in a model-independent way, each of them is fit with a spectral index $\gamma_{e^\pm}$ as

$$\phi_{e^\pm}(E) = C_{e^\pm} E^{\gamma_{e^\pm}} \quad \text{or} \quad \gamma_{e^\pm} = d[\log(\phi_{e^\pm}(E))]/d[\log(E)] \tag{3.1}$$

(E in GeV and $C_{e^\pm}$ are normalization) over a sliding energy window, where the width of the window varies with energy to have sufficient sensitivity to determine the spectral index. The resulting energy dependencies of the fitted spectral indices are shown in Figure 4, where the shading indicates the correlation between neighboring points due to the sliding energy window.

The differing behavior of the spectral indices versus energy indicates that high-energy positrons have a different origin from that of electrons. The underlying mechanism of this behavior can only be ascertained by continuing to collect data up to the TeV region (currently, the largest uncertainties above $\sim$200 GeV are the statistical errors) and by measuring the antiproton-to-proton ratio to high energies. These are among the main goals of AMS.

In conclusion, the electron flux and the positron flux each require a description beyond a single power-law spectrum. Both the electron flux and the positron flux change their behavior at $\sim$30 GeV, but the fluxes are significantly different in their magnitude and energy dependence. Between 20

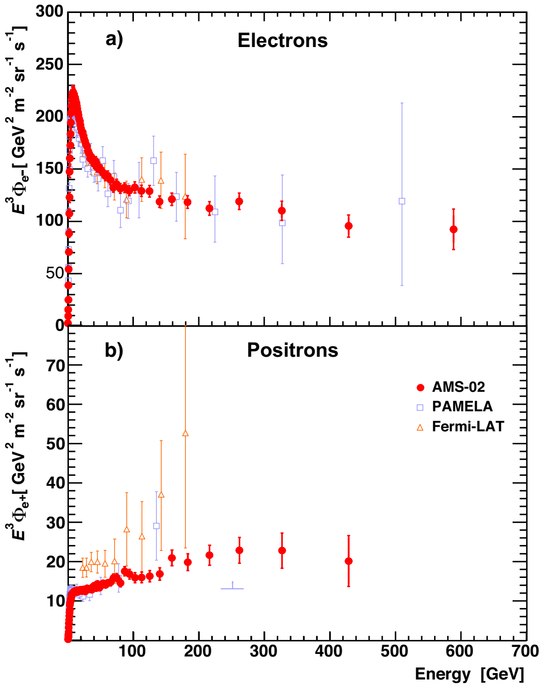

Figure 2: The AMS (a) electron and (b) positron fluxes, multiplied by E^3. Statistical and systematic uncertainties of the AMS results have been added in quadrature. Also shown are the most recent measurements from PAMELA [9] and Fermi-LAT [10].

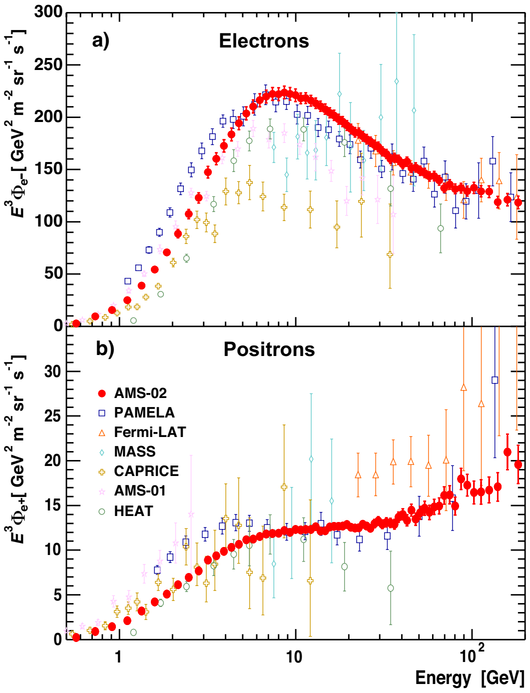

Figure 3: Detailed AMS (a) electron and (b) positron fluxes, multiplied by E^3, up to 200 GeV, with earlier measurements by PAMELA [9], Fermi-LAT [10], MASS [11], CAPRICE [12], AMS-01 [13], and HEAT [14].

and 200 GeV, the positron spectral index is significantly harder than the electron spectral index. These precise measurements show that the rise in the positron fraction is due to the hardening of the positron spectrum and not to the softening of the electron spectrum above 10 GeV. The determination of the differing behavior of the spectral indices versus energy is a new observation and provides important information on the origins of cosmic-ray electrons and positrons.

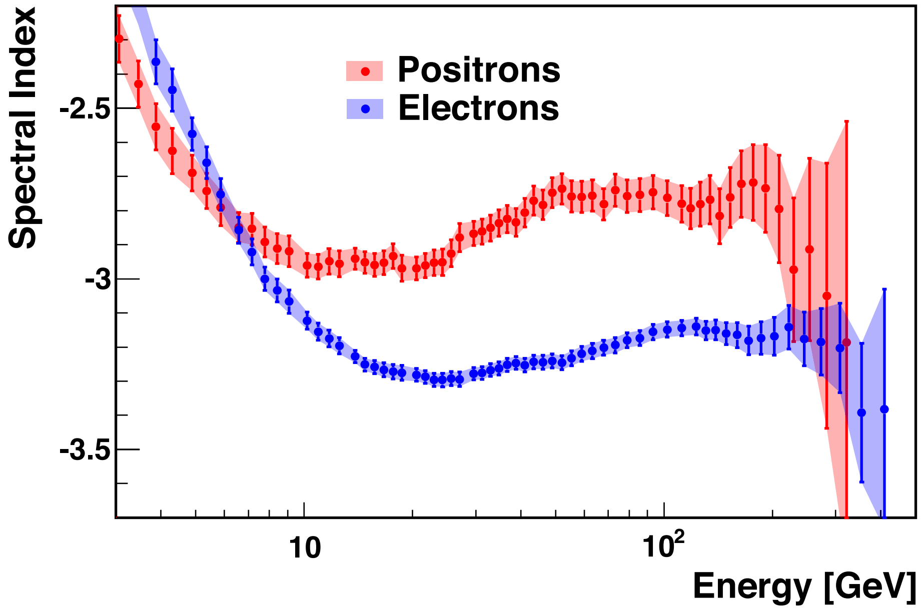

Figure 4: The spectral indices of the electron flux γ_{e^-} and of the positron flux γ_{e^+} as a function of energy. The shaded regions indicate the 68 % C.L. intervals including the correlation between neighboring points due to the sliding energy window.

References

[1] M. Aguilar *et al.*, Phys. Rev. Lett. **110** (2013) 141102;
L. Accardo *et al.*, Phys. Rev. Lett. **113** (2014) 121101.

[2] M. Turner and F. Wilczek, Phys. Rev. **D42** (1990) 1001;
J. Ellis, 26th ICRC Salt Lake City (1999) astro-ph/9911440.

[3] V. Vagelli, in proceedings of **EPS-HEP** (2015), PoS(EPS-HEP2015) 613.

[4] M. Aguilar *et al.*, Phys. Rev. Lett. **113** (2014) 121102.

[5] A. Kounine, Int. J. Mod. Phys. **E 21** (2012) 123005.

[6] B. Roe *et al.*, Nucl. Instr. Meth. **A 543** (2005) 577.

[7] S. Agostinelli *et al.*, Nucl. Instr. Meth. **A 506** (2003) 250-303;
J. Allison *et al.*, IEEE Trans. Nucl. Sci. **53** (2006) 270.

[8] C. Størmer, The Polar Aurora, Oxford University Press, London (1950).

[9] O. Adriani *et al.*, Phys. Rev. Lett. **111** (2013) 081102;
O. Adriani *et al.*, Phys. Rev. Lett. **106** (2011) 201101.

[10] M. Ackermann *et al.*, Phys. Rev. Lett. **108** (2012) 011103.

[11] C. Grimani *et al.*, Astron. Astrophys. **392** (2002) 287.

[12] M. Boezio *et al.*, Astrophys. J. **532**, (2000) 653.

[13] M. Aguilar *et al.*, Phys. Lett. B **484**, (2000) 10.

[14] M. A. DuVernois *et al.*, Astrophys. J. **559**, (2001) 296.